



POLITECNICO
MILANO 1863

RE.PUBLIC@POLIMI

Research Publications at Politecnico di Milano

Post-Print

This is the accepted version of:

M. Belan, R. Terenzi, S. Trovato, D. Uselli

Effects of the Emitters Density on the Performance of an Atmospheric Ionic Thruster

Journal of Electrostatics, Vol. 120, 2022, 103767 (12 pages)

doi:10.1016/j.elstat.2022.103767

The final publication is available at <https://doi.org/10.1016/j.elstat.2022.103767>

Access to the published version may require subscription.

When citing this work, cite the original published paper.

© 2022. This manuscript version is made available under the CC-BY-NC-ND 4.0 license

<http://creativecommons.org/licenses/by-nc-nd/4.0/>

Permanent link to this version

<http://hdl.handle.net/11311/1222447>

Effects of the Emitters Density on the Performance of an Atmospheric Ionic Thruster

Marco Belan^{a,*}, Raffaello Terenzi^a, Stefano Trovato^a, Davide Usueli^a

^a*Politecnico di Milano, Dipartimento di Scienze e Tecnologie Aerospaziali, 20156 Milano, Italia*

Abstract

A laboratory study on the performance of corona thrusters as a function of the spatial arrangement of the emitting electrodes is presented. The setup consists in arrays of emitters and collectors with independently adjustable spacings. This thruster is tested in different benches, for output velocity and direct thrust measurements. The measured velocity is also used to determine thrust by momentum balance, comparing it with direct readings. Electric measurements complete the dataset. The parameter space consists of two different collector spacings and several emitter spacings, with fixed interelectrode gap and voltage. Within this space lies an optimal collector-emitter spacing ratio 2:1.

Keywords: EHD propulsion, Atmospheric Ion Thruster, Corona Discharge, Ionic Emitters configuration

1. Introduction

Since the beginning of the aviation era, the development of increasingly efficient and powerful propulsive methods has been a major issue. Nowadays the trend is to move towards electrical propulsion systems in order to reduce carbon emissions. Among electric propulsion systems, the ionic thrusters have been successfully used for space applications for decades, however it is only recently that electrohydrodynamic (EHD) thrusters are emerging as a valid alternative for in-atmosphere propulsion [1, 2, 3, 4, 5, 6, 7]. Among their interesting properties there are high efficiency in terms of thrust-to-power ratio, absence of moving parts, low noise production, low maintenance and environmentally friendly energy source deriving from electric power consumption.

The basic configuration of an EHD thruster is composed by two electrodes, an emitter and a collector polarized by a suitable high voltage. The emitter needs to exhibit a very small curvature radius in order to increase the local electric field and produce ions. The easiest technology to create an emitter implies the use of metallic wires of radius smaller

*Corresponding Author

Email address: marco.belan@polimi.it (Marco Belan)

than $100\text{ }\mu\text{m}$, although metal pins [1] and thin metal tapes [4] are also used in literature. The collector instead consists of a macroscopic object, very often a metal cylinder with radius in the cm range. An electric field between the two electrodes ionizes the gas surrounding the emitter, creating a corona discharge and providing a drifting motion to the non-neutral molecules. While drifting, ions transfer momentum to the neutral molecules, thus accelerating the neutral air and creating thrust. Starting from these elements, different configurations followed along the years. The early EHD devices, called lifters [8], consisted in metal foils as collectors and small wires as emitters. Most studies aiming to provide a physical insight on EHD thrusters involve simple geometries such as the wire-cylinder configuration [2, 3, 9, 10, 11, 12], however the noteworthy devices which guarantee a sustained flight do not use such a geometry since cylindrical collectors produce non negligible aerodynamic drag. Better performance is generally achieved by means of slender, airfoil-shaped collectors: in fact, these electrodes are standard airfoils in the ion-propelled aeroplane designed by Xu et al. [13], while the ionocraft designed by Khomich and Rebrov [14] employed symmetrical drop-shaped collectors. The simultaneous influence of the collector shape on electric and motion fields is still an open field of research and indicates the need for further studies, including parametric optimizations [15]. A further degree of freedom in geometric design implies the use of multiple propulsion units. When multiple units are used they can be arranged to form thrust cells, as shown in Fig. 1 for simple wire-cylinder units.

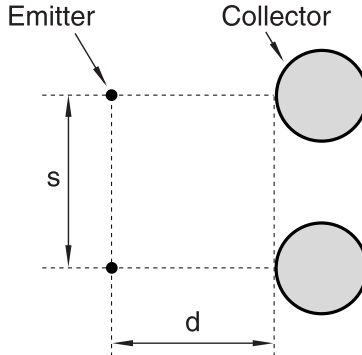


Figure 1: General illustration of a thrust cell and definitions of spacing s and gap d (emitters not to scale)

In this kind of thrusters, besides the gap distance d between emitters and collectors, it is possible to define a spacing s between adjacent electrodes of the same polarity. Throughout the EHD history, multiple thruster units were placed as in Fig. 1 on top of each other, creating thruster arrays [14, 16], or aligned in sequence creating multi-stage thrusters [13], in order to increase the overall propulsive force. Furthermore, the spatial arrangement of multiple emitters and collectors is not trivial. The simplest way to arrange them involves placing a single emitter for each collector in a periodic array. In the mentioned airplane [13] the electrodes pairs were directly aligned, i.e. placing

the emitters in front of the collectors (Fig. 2a), while the cited ionocraft [14] adopted a different configuration consisting of staggered electrodes (Fig. 2b), inspired by previous studies [17]. Further different approaches are possible, and a systematic investigation about electrodes alignment has yet to be presented.

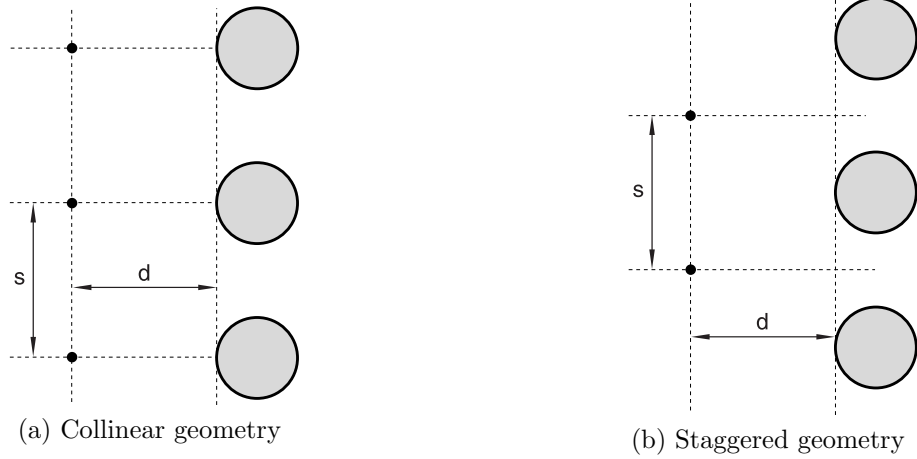


Figure 2: Two important cases of electrodes positioning in the state of the art.

For the above reasons, the present work is focused on the study of multiple emitters configurations, starting from the plausible hypothesis that the number of emitters in a given length (or emitters density) facing a collector should have an impact on the propulsive force, and looking at future applications in which the emitting system could become a grid of electrodes. To this purpose, several tests with different spacings between emitters were performed while keeping fixed collectors arrays. In order to limit the collector geometry influence on results and perform the experiments in a reasonable time, only two spacings between collectors were adopted, together with a constant gap d . All the configurations are compared in terms of thrust and related parameters such as thrust-to-power ratio and thrust density (referred to the front area of the device), by exploiting velocity field as well as direct thrust measurements.

This article is organized as follows: in Section 2 the experimental setups are presented. Section 3 shows how measurements were acquired and processed, together with the description of the analytical model used to estimate thrust through momentum conservation. Section 4 presents all the results obtained, finally Section 5 concludes the work.

2. Experiment Setup

In this work two experimental setups were employed: a test rig already used in [15] for velocity measurements through a miniature Pitot probe was modified introducing a new support to easily accommodate a variable number of emitters (Fig. 3); a new structure

was designed and built to directly measure thrust by means of load cells (Fig. 4). Both systems can host different numbers of emitters and collectors, including the previously studied cases [15] as a comparison. In the present experiments there are 5 airfoil-shaped collectors, in order to create an array that guarantees a good approximation of the periodic conditions on the outflow near the central collector. The two setups can work on replicas of the same propulsion systems thanks to the extensive use of rapid prototyping for several components. This ensures to perform velocity and force measures on the same electrodes geometries allowing direct comparisons of the results. The results are analyzed in a reference system common to both setups, with axes referred to the airfoil-shaped collectors, thus the directions are x (chordwise), y (normal to the airfoils chords) and z (spanwise).

For the velocity measurements, a Pitot probe made of Pyrex with an internal diameter of 0.5 mm and external diameter of 2 mm was used. The probe is the same as in [15], however in this work it is moved on a yz -plane normal to the thruster outflow instead of a 1D domain, in order to obtain a more complete description of the field of motion. The traversing system is a double linear positioning device with an accuracy of ± 0.1 mm. The pressure between the tip and the external reference is measured by a differential transducer GE Druck LPM 9000 series with range from 0 to 10 Pa and accuracy of $\pm 0.1\%$ of full scale.

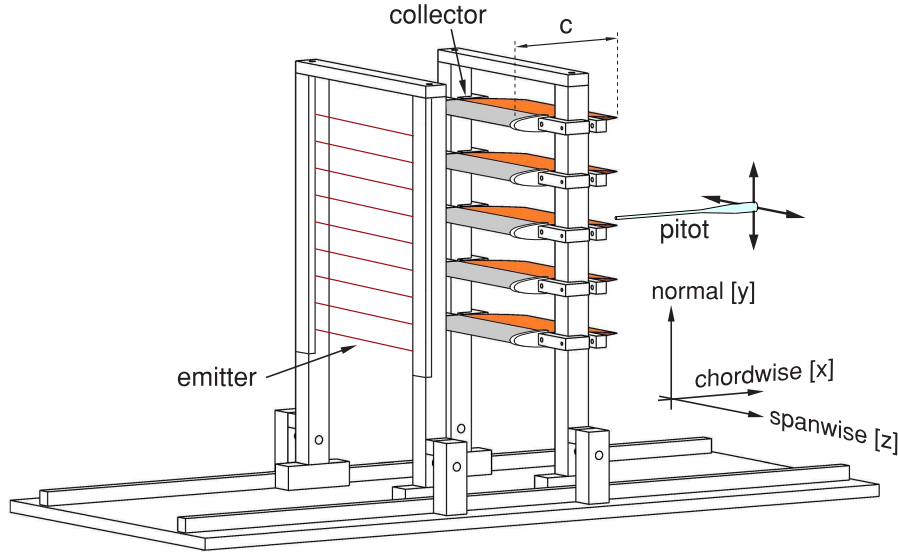


Figure 3: Setup for flow velocity measurements.

In both setups, a constantan wire with a diameter of $30 \mu\text{m}$ is used for the emitters array. The wire is wound around lateral arrays of pegs to form a serpentine grid, and the sections in which the wire goes around the pegs are covered such that they do not participate in the ionization process. As a result, the emitting system consists of a grid

of parallel wires, spanwise-oriented, with adjustable spacings in discrete steps, starting from the smallest available of 2.5 mm. In all the tests, the 5 collectors are 3D-printed NACA0010 airfoils, coated with aluminum on their front parts, in such a way as to obtain an electric behaviour with negligible differences with respect to a totally metallic surface. The emitters are connected to a positive high voltage source (Glassman PS/FC20R06) while the collectors are electrically grounded. The active span (exposed length) of the electrodes is $b = 140$ mm and the chord of the collectors is $c = 100$ mm. In the mentioned previous experiment [15] the gap effects were found to be qualitatively in accordance with known scaling laws, thus the gap in this work was fixed at $d = 20$ mm.

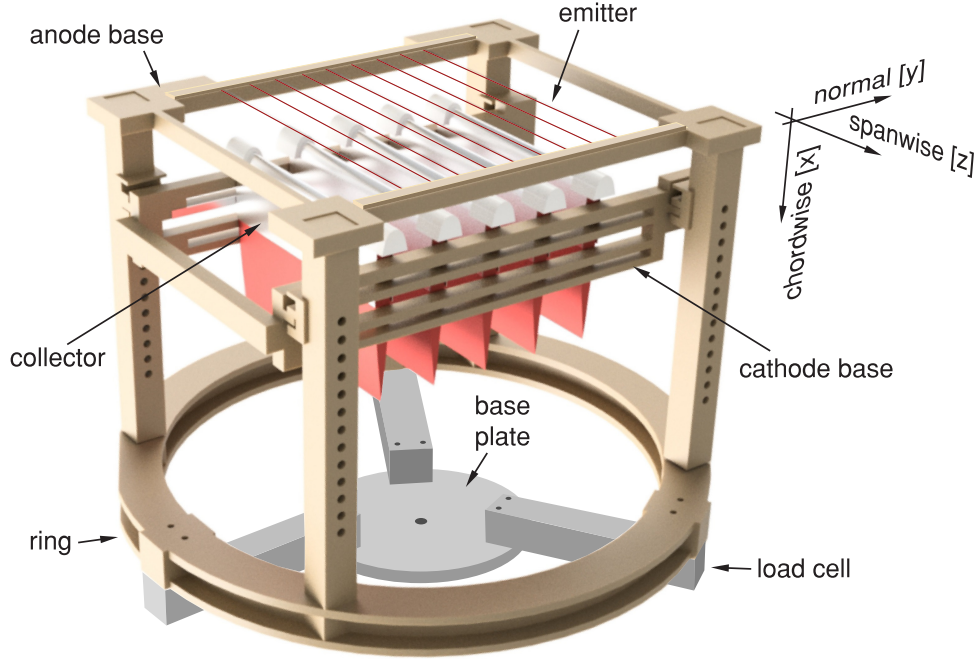


Figure 4: Setup for thrust measurements.

The details of the setup for direct thrust measurements are visible in Fig. 4. All the components are 3D printed and made of insulating materials such as Acrylic Styrene Acrylonitrile (ASA) and Polylactide (PLA). The main components are an anode base, a cathode base and a ring. The anode base houses the emitters system with adjustable spacings as explained above. The cathode base houses the collectors, mounted on rails which allow for a continuous spacing adjustment, since all the airfoils have copper brushes on their sides to connect them to a metal ground strip on the side of the base. The two bases are connected through bars that allow to vary the gap between the electrodes in 10 mm steps.

The requirements on accuracy pose strict constraints on the maximum load and as such, in order to support the weight of the structure, a number of 3 identical load cells

HBM PW6C is used. These are disposed in a radial configuration with equal angular spacing, connected to the propulsive system by means of the ring coupler visible in Fig. 4. On their opposite sides, the cells are mounted on a rigid base plate, which is in turn connected to a laboratory table with insulating surface. The entire structure is enclosed within a box that protects the thruster and the operators while allowing the necessary airflow: thanks to horizontal openings close to the table, the airflow directed towards the table is radially deflected. The distance between the emitters and the table surface is 282 mm, i.e more than 14 times the gap d ; correspondingly, the distance between the trailing edge of collectors and the table is 162 mm = 1.62 c , so that the flow deflection occurs at such a distance from the thruster that the local flow around it is not affected. This property was also verified by means of a moving plate behind the setup of Fig. 3. The maximum load of each cell is 7.5 N each and the accuracy is ± 1 mN. However, the overall uncertainty in thrust measurements turns out to be larger because of the mechanical couplings of the system and the error sources, as explained in detail in §3.3. The base plate and the metal bodies of the load cells are grounded, and a custom built signal conditioner with high rejection to EM disturbances is used to amplify the mV-range signals of the cells. The details of this device are described in Appendix A.

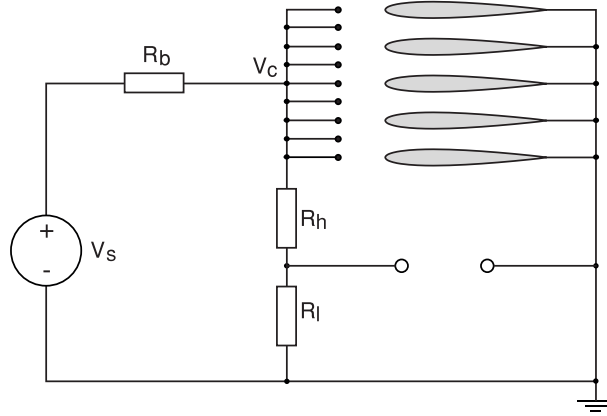


Figure 5: Electric circuit diagram.

Both setups share the same high voltage power supply which provides a positive DC voltage of $V_s = 20 \pm 0.03$ kV through a ballast resistance of $R_b = 0.996 \pm 0.003$ M Ω . The complete electric setup is shown in Fig. 5. During the tests the voltage V_c between the electrodes and the current I_{tot} flowing in the circuit are continuously measured. V_c is measured using a voltage divider with an output voltage ratio of 10^{-3} and a total resistance $R_h + R_l = 152.9$ M Ω . This value is larger than the apparent resistance of the inter-electrode gap system, which is in the order of 40 M Ω during normal operation. The resistive devices like ballast and voltage divider are purposely built making use of Vishay VR68 High Voltage resistors. I_{tot} is measured by means of the ammeter integrated in the power supply unit, with an accuracy of ± 0.005 mA, and the thruster current I_c is

determined by subtracting the current flowing into the voltage divider. The corresponding uncertainty on the power consumption is $\pm 0.1\text{W}$, in the order of 1/100 of the measured power, however this value only holds in short-term measurements, i.e. for tests repeated immediately one after the other. The mid-term repeatability (on different days) is worse, presumably because of the accumulation of contaminants on the emitting wires, that may create local variations of their curvature radius with a detrimental effect on the ion production, as also evidenced for different corona devices [18]. As a consequence, the statistic on power measurements gives deviations larger than $\pm 0.1\text{W}$, which affect the error bars in thrust-to-power results, as reported in §4. Wire emitters are a practical solution to create ions in these thrusters, particularly in this experiment where their configuration is changed several times, however their long term behaviour is affected by contamination, sputtering and aging. This will require further studies in future, for instance considering for ion generation more robust devices of larger cross section. The electrical transparency of the system and the leakages have been assessed by some tests performed by inserting shunt resistors in different branches of the circuit. These tests revealed that occasional undesired leakages appear as fast current peaks (less than 100 ns) superimposed to the typical value, but they do not significantly contribute to the power measures. The results are consistent with the uncertainty on power measurements and the ratio of emitters current to collectors current is close to unity with uncertainty of ± 0.001 .

All the output signals coming from the instrumentation are acquired using an oscilloscope Tektronix DPO4034B, whose input impedance has been taken into account in all the measurement procedures. For velocity measurements, the signal of the pressure transducer is read on a time window of 20 s with a 5 kHz sampling rate, while for thrust measurements the signal from the conditioner is read on a time window of 2 s with sampling rate of 50 kHz. These bandwidths are much larger than required for the measures presented in this work, however they have been selected in order to have a clear characterization of the disturbance spectra. The above settings are also used to acquire the corona voltage signal during standard tests, whereas in case of troubleshooting the electric measurements are performed at much higher sampling rates.

3. Experimental procedures and data processing

The results presented in this work derive from both velocity and load measurements. The first ones were acquired in order to analyze the aerodynamic behaviour of the thruster and may also provide a thrust estimate through conservation laws. The net force is measured directly by means of the load cells, with higher accuracy. The key evaluation metrics, the test procedures and the relations between different kinds of measures are presented in this section.

3.1. Performance parameters

The most common parameters considered in EHD studies along with the net thrust are the thrust-to-power ratio and the thrust density: the first is an important efficiency

index and the second provides a relationship between propulsive force and thruster size.

In detail, the thrust T is measured in this experiment by two methods (direct and momentum conservation), together with the electric quantities. This leads to determine a thrust-to-power ratio T/P referred to the power consumption $P = V_c I_c$. A simple theoretical model [10] gives an estimation of the thrust in absence of drag as $T = I_c d/\mu$ where μ is the ion mobility. In presence of drag, the net thrust can be generalized by including a term θ which accounts for the losses [19], leading to $T = (1 - \theta)I_c d/\mu$. The corresponding thrust-to-power ratio becomes $T/P = (1 - \theta)d/(\mu V_c)$. As a reference, peak values larger than 100 N/kW were measured in laboratory [10], while common values of the state of the art devices range from 5 to 25 N/kW [3, 20]. The thrust density can be referred to the volume or to a reference area of the thruster: in this work, the thrust density ratio T/A is referred to the thruster frontal area. Common values for this parameter are in the order of 5 N/m².

3.2. Pressure-based velocity measurements

Pressure measurements were performed along an yz -plane downstream of the thruster, in order to determine the longitudinal velocity $u(y, z)$, oriented in the x direction. The measurement plane is sketched in the general scheme of Fig. 6, which presents the nomenclature adopted for the experimental procedures and the data processing, evidencing the 4 cells between collectors and the lateral regions of the propulsive system (above and below it in Fig. 6), together with the control volumes used for momentum balance in §3.4 and the relevant surfaces. The cells height and span are defined by the collectors spacing and span. In this work, the velocity measurement plane was located at $x = 2$ mm downstream of the thruster. In particular, measurements were taken for the outer and central cells (1 and 2), together with the region 0 outside the outer airfoil to include this part of the flow field and account for extremity effects. The remaining cells are assumed to feature a symmetrical behaviour. The details about velocity measurements, including their accuracy, are presented in Appendix B.

3.3. Thrust measurements

In the thrust measurement setup, this force is directly read by means of the load cells mentioned in §2, which bear the whole structural weight of the system shown in Fig. 4. When the supply voltage is applied to the emitters, the net force exerted by the thruster, due to ionic wind, causes a readable reduction in the load applied to the cells. Before each test campaign, cells calibration is performed by means of accurate sample weights in order to adjust zero and gain in each channel of the signal conditioner. The basic principle for thrust measure is expressed as

$$T = F_{off} - F_{on} \quad (1)$$

where F_{off} and F_{on} are respectively the loads with unpowered and powered thruster. In practice, this concept translates into a careful procedure, defined to minimize the measurements error, as described in Appendix C.

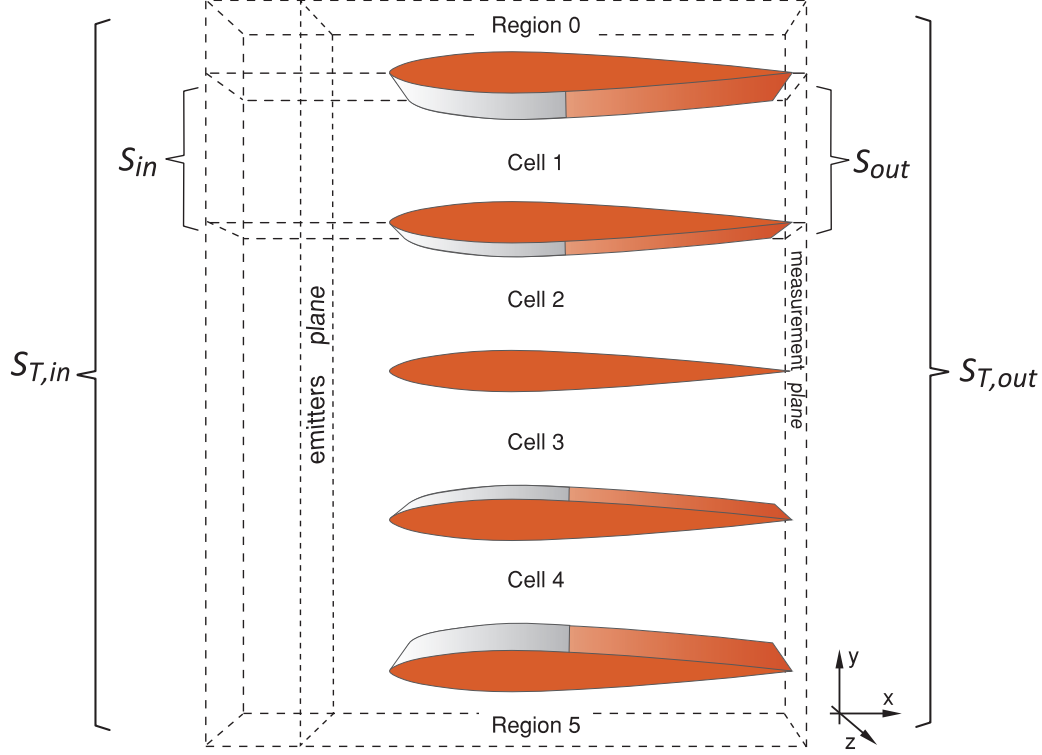


Figure 6: Nomenclature for experimental procedures and control volumes for analytic models, with reference system.

3.4. Thrust and momentum balance

In a previous work employing the same setup for velocity measurements [15], the thrust was estimated from velocity profiles using a simplified 2D analytical model and exploiting momentum balance, starting from integral Navier-Stokes equations including an electric term, as recalled in Appendix D. That model is revisited here, since in this work it is possible to compare direct thrust readings and momentum balance results obtained through a better characterization of the field of motion.

The chance to measure a complete velocity field along a cross section of the outlet flow downstream of the thruster (Fig. 6) makes this field available as $u(y, z)|_{out}$, and permits a 3D reformulation of the momentum conservation on a volume enclosing the thruster:

$$T = \iint_{S_{T,out}} \rho u^2 dydz - \iint_{S_{T,in}} \rho u^2 dydz + (p_a - p_{in}) S_{T,out} , \quad (2)$$

where ρ is the air density, u the velocity, p_a and p_{in} the atmospheric and inlet pressure respectively. The integration domain is shown in detail in Fig. 6 and it is extended considering also the contribution from the outer regions, external to the four main cells of the test rig. For simplicity, the outer regions height in the y direction is half of the inner

cells spacing, thus adding a complete cell to the overall domain. Here the integrals are no longer computed along lines as in [15], but on boundary surfaces, thus $\mathcal{S}_{T,out}$ and $\mathcal{S}_{T,in}$ evidenced in Fig. 6 represent respectively the entire outlet and inlet areas of the thruster volume, supposed to be equal. For an array consisting of n_c identical cells, Eq. (2) may be simplified into:

$$T = n_c \left[\iint_{\mathcal{S}_{out}} \rho u^2 dydz - \iint_{\mathcal{S}_{in}} \rho u^2 dydz + (p_a - p_{in}) \mathcal{S}_{out} \right] + T_{outer} \quad (3)$$

where n_c corresponds to the number of internal cells of the thruster, \mathcal{S}_{out} is the single cell downstream area and \mathcal{S}_{in} is the upstream one. T_{outer} is the thrust contribution of the two outer half cells, determined in a similar way but featuring a different velocity distribution, bounded by a single solid surface. Eq. (3) is a very good approximation for thrust when n_c is large and the output field $u(y, z)|_{out}$ may be regarded as a periodic field. Obviously, the importance of term T_{outer} becomes negligible as n_c grows. However, in the results section it will be shown that even in the present case, where $n_c = 4$, this formula can be used to obtain a good approximation of the actual thrust, known here thanks to the load cells.

In detail, evaluation of T requires the calculation of the following terms in Eq. (3). The first integral in brackets is straightforward since $u = u(y, z)|_{out}$ is known on the surface \mathcal{S}_{out} . Concerning the inlet term, as in [15] upstream velocity is estimated exploiting inlet-to-outlet mass conservation, thus the inlet velocity u_{in} is expressed as a constant value on surface \mathcal{S}_{in} . Finally, the pressure term is the same as in Eq. (D.1) of the previous model and is expressed as the difference between ambient pressure p_a and inlet pressure p_{in} , determined by the suction effect at the thruster inlet.

The proper use of this improved model requires the knowledge on the output plane of the longitudinal (chordwise) component of velocity u , which is measured here by a Pitot probe. This device is also sensitive to the transverse velocity components within a limited angular range, so that when measures are taken in the proximity of the trailing edges and in the outer domain regions this error is inevitably introduced. However, it is reasonable to assume that the angle between airflow velocity and chordwise direction is small, in the order of the trailing edge steepness (here less than 6°) over most of the span and thus in the present calculations the relevant effects have been neglected. Indeed, the results obtained by means of this model and presented in the following section turn out to be well comparable to the direct readings of the load cells.

3.5. Electrodes configurations

The two available setups allow to study a very large number of cases, even working with fixed gap $d = 20$ mm and voltage $V_s = 20$ kV, as anticipated in §2. The main objective of this work focuses on the effects of different numbers of emitters for a given collectors configuration, thus the key parameter is the emitters spacing. Each collectors configuration gives rise to a new and different experimental campaign, so in this work

two main configurations were chosen: one with NACA0010 collectors and spacing 25 mm, that offered the best T/A and T/P figures in a previous experiment on a set of different collectors and spacings [15]; another configuration adopts the same NACA0010 collectors but with spacing 35 mm, chosen after preliminary tests as a trade-off between achieving better absolute thrust and T/P figures and limiting the T/A decrease due to the larger front area.

As explained in §2, the emitting wires are held by anode bases with periodic pegs, that permit rapid changes of the emitters spacing but impose spacing variations in finite steps. In particular, two anode bases are available, one allowing emitters spacings $s = 2.5 + 5 i$ mm and another allowing $s = 5 + 10 i$ mm, with integer i . The tested configurations chosen according to these rules are presented in Table 1, including standard cases with equal numbers of emitters and collectors. Here the notation SC and SE is introduced to indicate the spacing of collectors and emitters respectively, writing in what follows short codes as SE15 instead of SE=15 mm for the sake of brevity. The reported configurations

Table 1: Tested configurations

SC [mm]	SE [mm]	SC/SE	Emitters No.	Periodic
35	35	1	5	yes
35	25	1.4	7	no
35	17.5	2	10	yes (*)
35	17.5	2	11	yes (*)
35	15	2.33	11	no
35	12.5	2.8	13	no
35	7.5	4.67	21	no
25	25	1	5	yes
25	15	1.67	10	no
25	12.5	2	11	yes
25	7.5	3.33	15	no
25	5	5	23	yes

(*): these configurations were tested with different alignments as explained in the body text

range from 5 to 23 emitters, providing an adequate number of test cases achievable within a reasonable laboratory time, thanks to the anode base system used to hold and easily reconfigure wires. The alignment of the emitters and collectors arrays has always been set ensuring symmetry with respect to the central plane of the whole system, i.e. the plane passing through leading and trailing edges of the central collector in Fig. 6. The two configurations SC35 SE17.5 indicated as (*) in Table 1 have been purposely introduced to explicitly examine the differences between collinear and staggered alignments represented in Fig. 2. The listed configurations also involve another effect, as reported in the last column of Table 1: in fact, the tested geometries turn out to be periodic or aperiodic,

as sketched in Fig. 7. A configuration is said to be periodic if the arrangement of the emitters in front of a thrust cell is the same for all thrust cells (Fig. 7a), otherwise it is called aperiodic (Fig. 7b). The effects on the overall performance turn out to be mainly due to the emitter spacing and not to the periodicity, as shown and discussed in the next section. In particular, the thrust mainly depends on the integrals of the velocity squared on the outflow domain, and is less influenced by the small local variations created by the specific emitter arrangements.

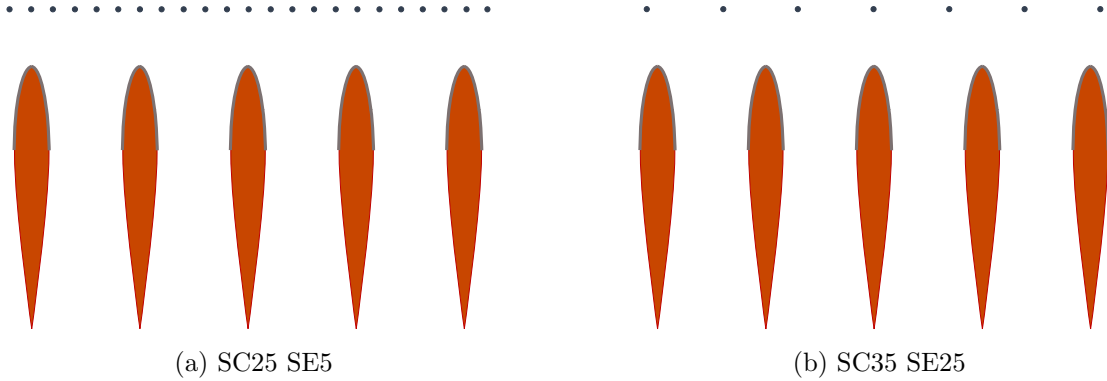


Figure 7: Examples of periodic (a) and aperiodic (b) configurations.

4. Results

4.1. Direct thrust measures and related parameters

The thrust measurements as function of emitters spacing are presented in Fig. 8. Considering overall thrust, the curves feature a similar behaviour: starting from the right with SC=SE configurations (spacing ratio 1:1), as the emitters spacing decreases, thrust increases. Then, after reaching a peak value the curves decrease. For both collectors spacings the peak value is obtained with the SC=2SE or 2:1 configuration. In the SC35 case, the generated thrust increases from a value of 48.5 mN using SE35 to 63.0 mN with SE17.5, providing an approximate 31 % gain. In the SC25 case, thrust increases from 40.0 mN with SE25 to 44.5 mN with SE12.5, which is approximately 11 % higher.

The main result here is the existence of a peak: above this value, an increase in the number of emitters leads to a thrust decrease. A possible explanation may involve the electric interaction between the components of the thruster, since in an EHD thruster, besides the obvious interaction between emitters and collectors, there is an interaction between the emitters themselves. If the emitters density (number of emitters per unit length) is progressively increased keeping a constant emitters-collectors gap d , it is reasonable to expect an asymptotic behaviour of the emitters array similar to an equipotential plate, leading to strong emitting regions only at the array borders. This is known as *shielding phenomenon*, generally favoured by a short emitters spacing SE with respect to the gap

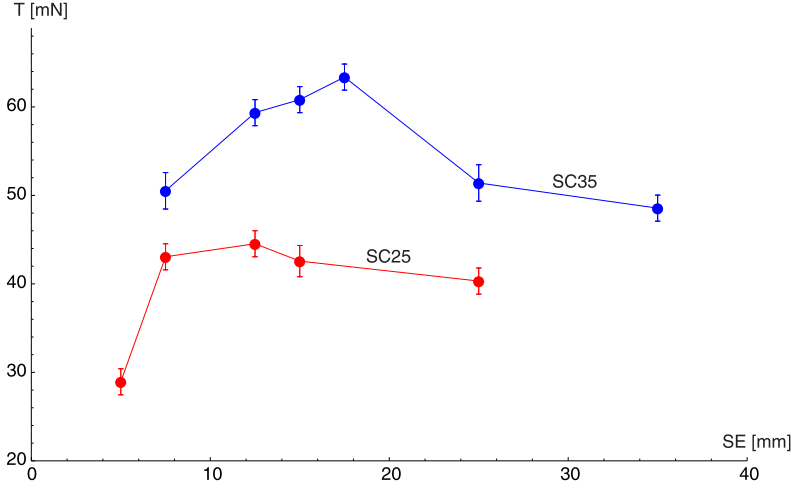


Figure 8: Thrust T vs emitters spacing SE for two different collectors spacings, SC25 and SC35.

d. When it takes place, for some emitters the corona inception may be inhibited so the emitters array works only partially. A recent study from Lemetayer et al. [21] describes in detail this phenomenon for a geometry with multiple wires facing a single cylindrical collector, revealing this 'plate behaviour' with strong emission only at the array ends for a dense system of emitters acting on a large gap d . In some configurations, also partial inceptions among emitters were observed at a certain supply voltage, which consequently needs to be increased in order to ensure a full ignition. As a general result, when additional emitters are placed in a given setup, the thrust does not generally scale with the emitters number and a careful geometric design is required. The phenomena above described may presumably explain also the trends observed in this work, where only the emitter spacing is changed for a given gap and collector structure, performing all tests at the same operating voltage, always reached by a slow ramp.

The thrust-density curves T/A (Fig. 9) feature a similar behaviour as the thrust curves, but involve the important effect of the scaling factor A , which is the frontal area of the thruster. The larger frontal area of the SC35 configuration ($A_{SC35} = 0.0168 \text{ m}^2$) with respect to the SC25 ($A_{SC25} = 0.0120 \text{ m}^2$) tends to lower the SC35 thrust density, however the increase in thrust for the case SC35 SE17.5 is large enough that this configuration remains more advantageous than any SC25 configuration.

Fig. 10 shows how the emitters density affects the thrust-to-power ratio T/P . This efficiency parameter is highly dependent on corona current, which in turn is very sensitive to experimental setup details as for instance emitter/collector misalignments, wire tension and insulators geometry at the airfoils tips. As such, the relative comparison between different configurations is more relevant than their absolute values. Considering all the tested configurations, the dependence of T/P on the emitter spacing is not strong, and the maximum observed variation of T/P is in the order of 10%: in particular, the variations

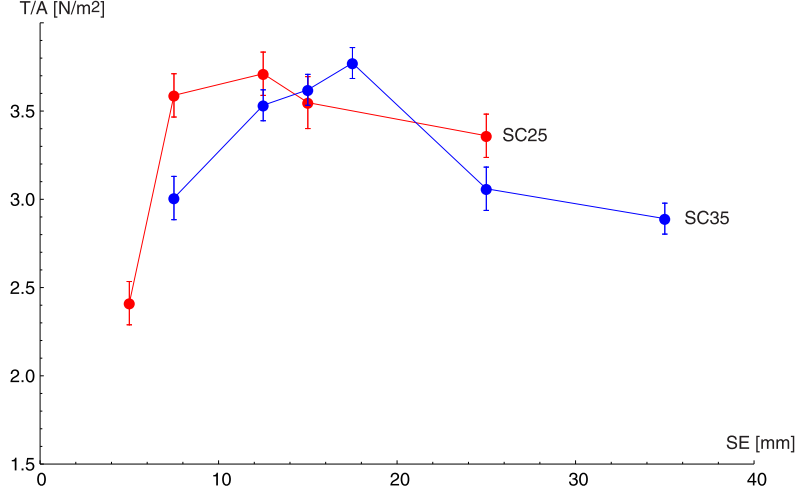


Figure 9: Thrust density T/A vs emitters spacing SE for collectors spacings SC25 and SC35.

of T/P for the SC35 set are greater than for SC25. On the left of the plot, both curves decrease as the emitters spacing is lowered: here the corona current decreases but thrust decreases even further, thus resulting in a lower T/P . The results also show that the 2:1 periodic configurations have higher thrust-to-power ratios with respect to the 1:1, even if the 2:1 values are not maxima of the T/P curves.

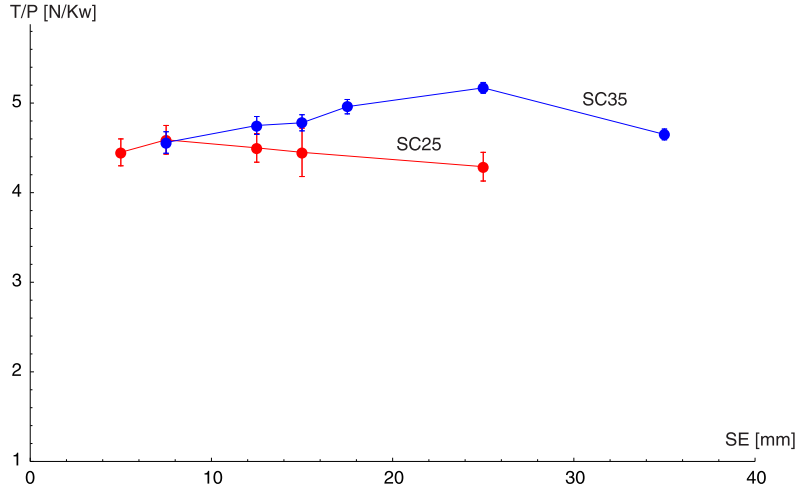


Figure 10: Thrust-to-power ratio T/P vs emitters spacing SE for collectors spacings SC25 and SC35.

The maxima, not very pronounced, are instead on the points SC35 SE25 and SC25 SE7.5: for these configurations the reason could lie in the absence of wires directly facing collectors, i.e. the electrodes positioning is similar to Fig. 2b rather than Fig. 2a. Thus, in these configurations the local emitter-collector distances are always larger than the gap

d , presumably reducing the local currents while giving good ionic wind and thrust levels as indicated by the previous data. The configurations SC35 SE25 and SC25 SE7.5 are aperiodic, but this is not a fundamental point, in fact it is possible to obtain similar effects also with periodic geometries having the same property, i.e. without wires in front of the airfoils. An example can be provided by testing the same configuration SC35 SE17.5 with different alignments, always satisfying the periodic condition, namely with collinear alignment as in Fig. 2a and with staggered alignment as in Fig. 2b. The collinear case, which is the one plotted in Figs 8 to 10, gives $T = 63.5$ mN, $T/A = 3.78$ N/m² and $T/P = 4.96$ N/kW whilst the staggered case gives $T = 60.5$ mN (-5%), $T/A = 3.60$ N/m² (-5%) and $T/P = 5.16$ N/kW (+4%). This shows that the staggered configuration leads to a slight improvement in T/P at the price of a small decrease of T and T/A .

In general, the measurements in this section show that the best configuration in terms of thrust and thrust density is SC = 2 SE or 2:1, for which the thrust-to-power ratio also increases its value with respect to the 1:1 configuration. Table 2 outlines the results for the 2:1 cases SC35 SE17.5 and SC25 SE12.5, comparing them with the corresponding 1:1 configurations.

Table 2: Performance comparison for 1:1 and 2:1 configurations.

SC [mm]	SE [mm]	T [mN]	T/P [N/kW]	T/A [N/m ²]
35	35	48.5	4.65	2.88
35	17.5	63.5	4.95	3.78
25	25	40.0	4.29	3.35
25	12.5	44.5	4.50	3.70

4.2. Output flow characterization

This section presents the velocity measures on the output flow, that are useful to characterize the field of motion, to investigate in detail the effects of periodic/aperiodic emitters and to test the new algorithm of §3.4 for calculating thrust from momentum balance, comparing the results with direct readings. Normal and spanwise velocity profiles were acquired downstream of the thruster for several configurations, on the half domain downstream of Region 0, cell 1, cell 2 as sketched in Fig. 6 (the remaining regions are assumed to have a symmetrical behaviour). A selection of velocity profiles and maps is presented in what follows in dimensional form, however dimensionless velocities can always be obtained introducing as reference velocity u_{ref} the airspeed given by an ideal thruster of cross-section A :

$$u_{ref} = \sqrt{\frac{I_c d}{\rho \mu A}}. \quad (4)$$

The present velocities range from 0 to 3 m/s, corresponding to $2.5 u_{ref}$ for SC25 configurations or $2 u_{ref}$ for SC35.

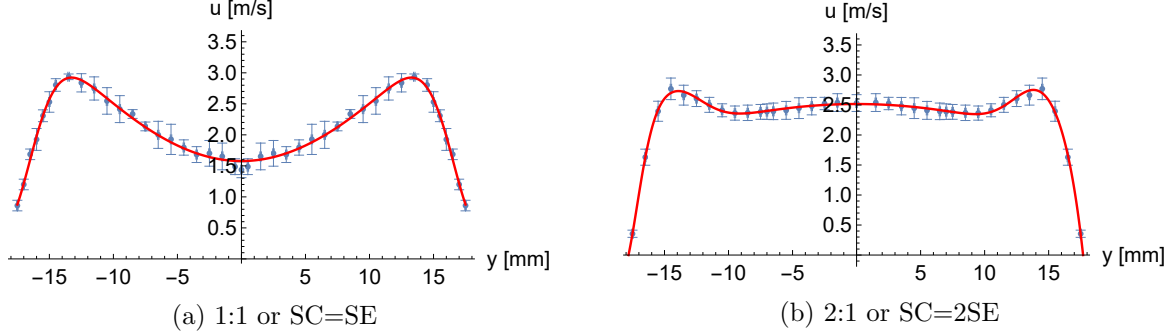


Figure 11: Comparison of normal velocity profiles downstream of cell 2 for SC35 spacing.

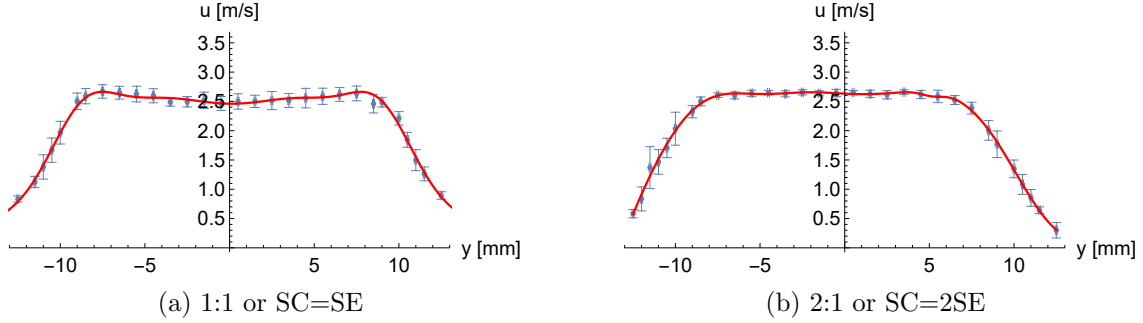


Figure 12: Comparison of normal velocity profiles downstream of cell 2 for SC25 spacing.

The first way to describe the outflow is to present normal sections of the field of motion, i.e. velocities $u(y, z_c)$ taken on the measurement plane of Fig. 6 along y direction at $z = z_c$, at the center of the airfoils span. These profiles would be constant with z only in a perfect 2D domain (infinite span); actually the dependence on z is very important, and will be presented later in this section.

The outflows $u(y, z_c)$ generated by the 2:1 configurations, more performing than the 1:1, are compared with the latter in Figs 11 and 12. These profiles are acquired downstream of cell 2, which may better mimic the periodic properties of the outflow of a large array. Concerning the SC35 geometries (wide collectors spacing), the velocity profile for the 1:1 case is a double jet-like flow with two peaks near the airfoils whereas for 2:1 it becomes a flatter curve with a further weak maximum in correspondence of the additional wire. For the SC25 geometries (narrower collectors spacing), the effect of the additional emitters are similar to the SC35 case but much weaker, and in both Figs 12a and -b the profiles resemble a channel-like flow, a property already evidenced [15] for flows bounded in narrow cells. The impact of the additional emitters in the 2:1 configurations can be evaluated through the momentum balance (2) and (3) of §3.4, where the modified velocity profiles affect the integral of $(u_{out}^2 - u_{in}^2)$ and the induced pressure term on a domain en-

closing the system. In fact, both the direct measures shown in Fig. 8 and the calculation from Eq. (3) indicate that a change of SC/SE from 1:1 to 2:1 leads to a thrust increase larger than 30 % for SC35 and 11 % for SC25 (a detailed comparison of thrust values from direct measures and momentum balance is presented at the end of this section).

Further observations can be made considering the error bars, that represent here fluctuation levels including also turbulent effects. As already described in a previous experiment [15], large fluctuations are expected in the center of cells with higher collectors spacing (Fig. 11a) while for narrower geometries (Fig. 12a) a channel-like flow should be encountered, leading to a more stable outflow, according to the lower Reynolds number based on the channel width (i.e. the collector spacing). In the present experiment, the introduction of additional emitters seems to reduce the fluctuations in the central zone, particularly in the SC25 case (Fig. 12b).

Another important aspect to consider is whether periodic and aperiodic emitter arrays impact overall performance differently. This analysis may start again from the periodic configuration of Fig. 11a: here two emitters face the cell at $y = \pm 17.5$ mm in the local frame centered on the cell itself. In Fig. 11b (always periodic), an additional emitter is placed at $y = 0$, and its effect is a global change in the profile shape rather than a sharp peak at the same $y = 0$ in the output velocity. In Fig. 12 similar considerations hold, but the changes are weaker due to the narrow spacing of the SC25 cell.

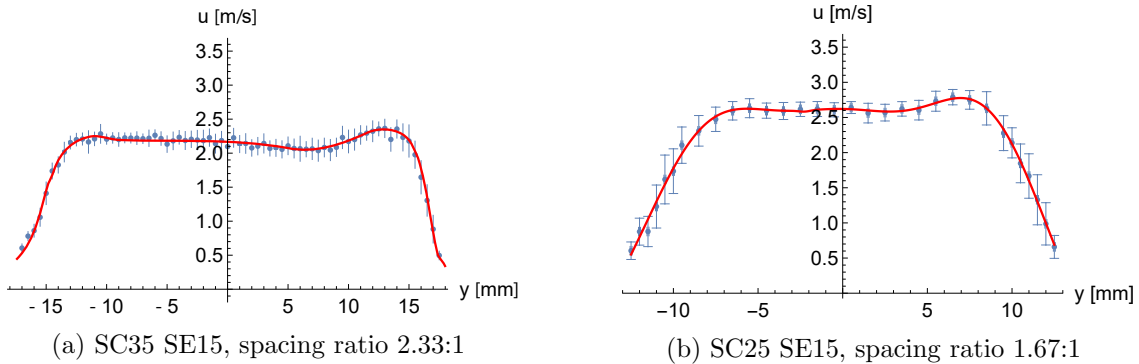


Figure 13: Normal velocity profiles downstream of cell 2 for aperiodic configurations

In Fig. 13 two velocity profiles with aperiodic configurations are presented, namely the cell 2 for SC35 SE15 (spacing ratio 2.33:1) and SC25 SE15 (spacing ratio 1.67:1), which share the same emitter spacing. In Fig. 13a, 3 emitters face the cell, corresponding in the local frame to $y = -17.5$ mm (aligned with the collector chord), -2.5 mm and $+12.5$ mm. The emitting system determines the velocity profile in its entirety, but only a weak trace of the 3rd wire effect ($+12.5$ mm) is visible as a mild peak in the velocity curve. Similar considerations hold for the case in Fig. 13b, where the emitters are located at $y = -5$ mm and $+10$ mm and their specific traces are difficult to distinguish.

Comparing Fig. 13a to Fig. 11a the main effect of the 2.33:1 configuration appears as a flatter velocity profile with respect to the 1:1, as happens for the 2:1 case of Fig. 11b; correspondingly, even for the 2.33:1 case the effect is a thrust increase, but less than for 2:1, as can be seen in Fig. 8. In general, in this experiment the aperiodic emitter arrangements result in slightly asymmetric flow fields on the cells outputs, however interpreting this property according to the momentum transfer, the small local effects do not significantly affect the integrals in Eq. (3), which are more dependent on the emitters spacing. This should be considered the main parameter in setting the thruster performance in this study and, more generally, would always be the main parameter in a large array with tens of electrodes distributed on a length well larger than the least common multiple of SE and SC.

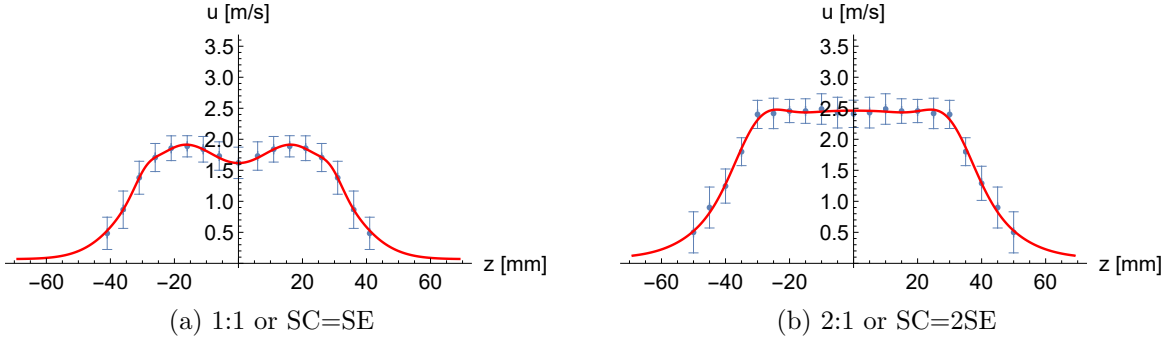


Figure 14: Comparison of spanwise velocity profiles downstream of cell 2 for SC35 spacing.

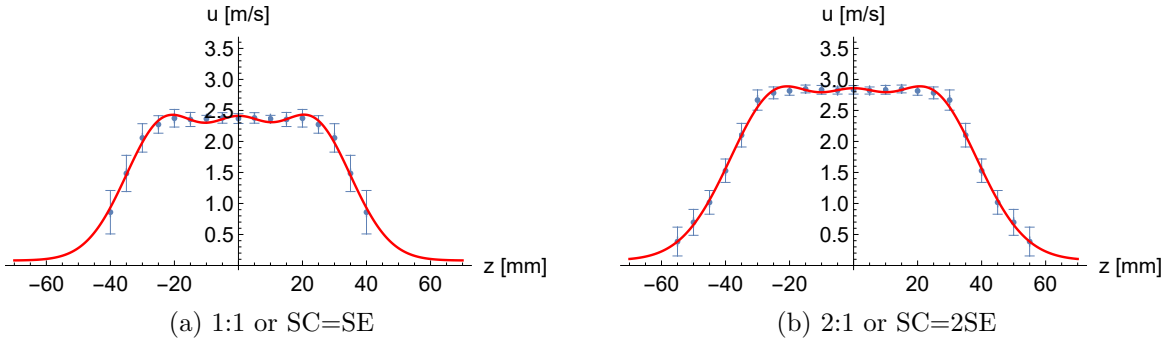


Figure 15: Comparison of spanwise velocity profiles downstream of cell 2 for SC25 spacing.

A further way to characterize the outflow is to examine the spanwise sections of the velocity field, i.e. the profiles $u(y_i, z)$ taken on the measurement plane of Fig. 6 along z direction at a given coordinate y_i . Here these profiles will be presented at $y = y_c$, a position equidistant from the trailing edges of two adjacent collectors. In Figs 14 and 15,

these were taken downstream of cell 2 for the 1:1 and 2:1 configurations already examined along the normal direction y . As is natural in a 3D domain with finite span, the velocity field exhibits a spanwise profile, which decays to very low values at the airfoils ends. Moreover, the profiles are also influenced by the configuration under test. The main difference between the 2:1 and the 1:1 configurations is that in the former the velocity decay occurs closer to the airfoils ends, making the system effective over a wider span. Another noteworthy difference between 1:1 and 2:1 is in the shape, in fact 1:1 profiles are less uniform along z , with local peaks that tend to disappear in the 2:1 configurations. This is particularly evident for the SC35 case, but is visible also for the SC25.

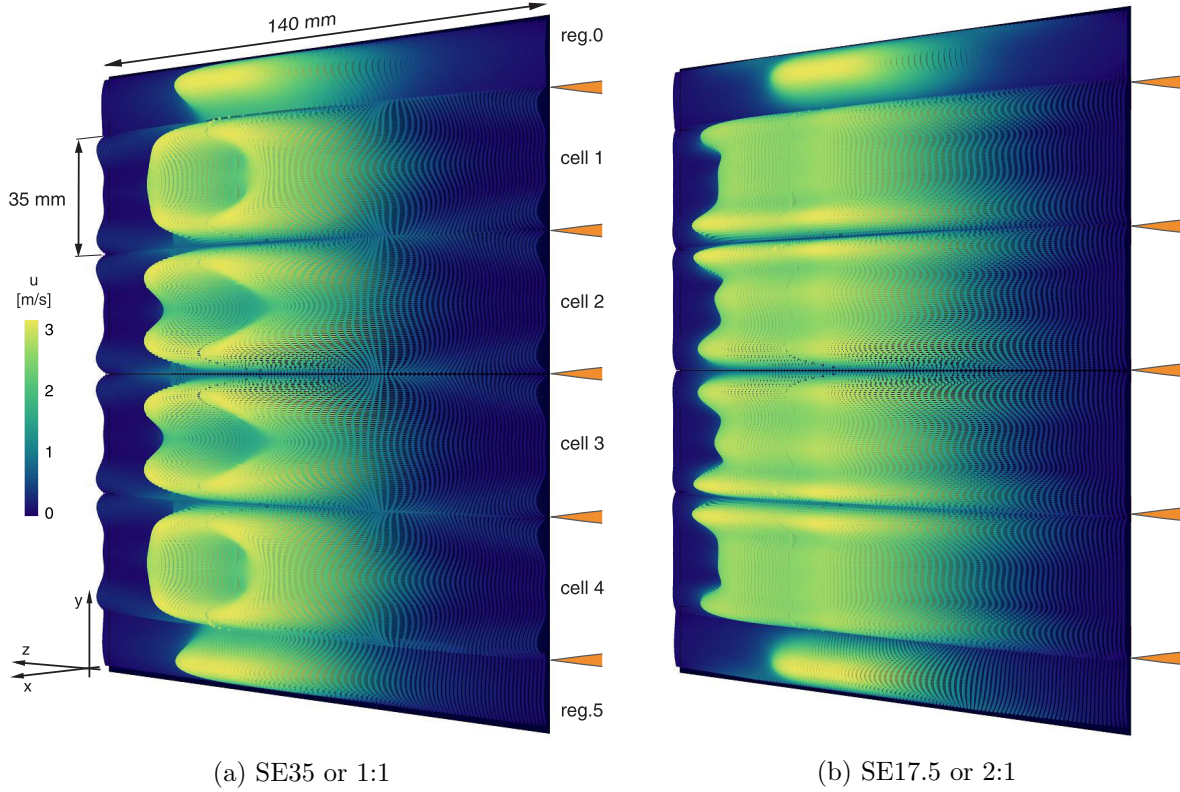


Figure 16: Complete velocity field $u(y, z)$ for SC35 spacing and two emitters spacings.

A general map of the velocity field, although more complicated to read, can be presented to give an overview of the properties described above and also to reveal further details. This is done for SC35 spacing in Fig. 16a and -b, representing the 1:1 and 2:1 case, respectively. A first look at the figure qualitatively shows how each cell contributes to the overall thrust. It is evident that the contributions of cell 1 and cell 2 (or 3 and 4 by symmetry) are similar. Fig. 16 also suggests that the two central cells (2 and 3) are a good representation of a periodic outflow, inherently confirming that the use of at least 5 collectors may represent a periodic field near the central zone.

Table 3: Thrust comparison between load cell readings and momentum balance models.

SC [mm]	SE [mm]	T [mN]		
		direct read	Eq. (D.1)	Eq. (3)
35	35	48.5	71.0 (+46%)	46.5 (-4.1 %)
35	17.5	63.5		65.0 (+2.2 %)
25	25	40.	57.5 (+44%)	39.0 (-2.5 %)
25	12.5	44.5		44.5 (0. %)

A quantitative confirmation comes from the evaluation of thrust through momentum balance as in §3.4, using Eq. (2) for each cell or region separately: in Fig. 16a this gives $(T_0, T_1, T_2) = (2.75, 9.25, 10.25)$ mN for region 0, cell 1, cell 2 respectively, with resolution 0.25 mN; in Fig. 16b the corresponding values are $(T_0, T_1, T_2) = (1.5, 14.0, 15.5)$ mN. The small differences between T_1 and T_2 lead to test Eq. (3) to obtain the total thrust from the velocity field under periodic conditions, i.e. as a sum of n_c contributions corresponding to cells of a periodic array of collectors, plus the contributions of the outer regions. In the present case, the method implies calculations of integrals on 4 replicas of the cell 2 field plus 2 identical outer regions. The results are presented in Table 3, where the thrust from momentum balance models is reported along with the percentage error (in brackets) with respect to the direct reading values. The table also includes the thrust obtained from Eq. (D.1), which is the simplified 2D model introduced in a previous work [15]. It is found that the previous model overestimates thrust, while the enhanced 3D model of Eq. (3) effectively matches the direct thrust measurements with a higher accuracy, since it accounts for the finite span of the collectors and the relevant changes in the velocity field.

5. Conclusions

The topic of this work was the investigation of multiple emitters configurations in an atmospheric EHD thruster. The main parameter varied during the experiments was the spacing between multiple emitting wires. In order to perform the study in a reasonable time, an affordable parameter space was defined by setting a fixed emitters-collectors gap of 20 mm and choosing two collectors systems with the same electrodes shapes (NACA0010 airfoils with 100 mm chord) and spacings of 25 and 35 mm. For each collectors system the emitters spacing has been varied, directly measuring thrust and also acquiring velocity measures downstream of the thruster. All the tested geometries were compared in terms of net thrust produced, thrust-to-power ratio and thrust density.

Starting from a standard collinear configuration (same spacing for aligned emitters and collectors), the introduction of additional emitters increases all the performance parameters previously mentioned: for both the collectors systems, the best configuration results in a 2:1 spacing ratio, i.e. two emitters for each collector, while a further reduction

of the emitters spacing (increase in the emitters density) degrades performance. This is presumably due to a shielding effect which prevents the creation of the optimal electric field between emitters and collectors arrays. In particular, the values of thrust and thrust density increase by an approximate 30% for the best configuration under test, corresponding to the larger of the two collector spacings. The increase of thrust due to the optimal spacings ratio in this case is presumably reinforced by the larger distance between collectors, which reduces friction losses.

This work also includes a detailed comparison between direct measures of thrust and analytical models providing thrust by means of momentum balance, based on velocity measurements. It turns out that a proper comparison requires the consideration of the flow in its three-dimensionality, accounting for the finite span of the electrodes besides the other relevant length scales. When used under these conditions, fluid dynamics diagnostics can provide global performance parameters as well as a local characterization of the field of motion at the same time.

The emitters arrays under test included periodic as well as aperiodic configurations. In general, in this experiment the main factor affecting performance turns out to be related to the velocity squared downstream of the thruster through an integral relation, mainly determined by the emitters spacing, and the local differences observed comparing periodic and aperiodic emitter arrangements do not seem to produce important effects.

Although the general validity of these results is limited by the working conditions on fixed gap and on two collector spacings, the properties outlined above could be helpful in future designs of thrusters with emitting grids as ionizing devices and large arrays of airfoils as collectors.

Appendix A. Electronics for thrust measures

The signals from the 3 load cells are transferred to a self-built signal conditioner through shielded balanced cables connected to differential inputs. The conditioner has 4 channels making use of high performance operational amplifiers with common mode rejection ratio (CMRR) of 126 dB and very low noise ($3 \text{ nV/Hz}^{1/2}$ in the kHz range and not larger than 80 nV_{pp} at very low frequencies). The amplifiers have also a bandwidth extending to the MHz range, not needed in this application. Each channel also provides stabilized power supply to the Wheatstone bridge inside the relevant cell. These features, together with a heavily shielded case and a general connection of ground lines without loops (star topology) ensure a high rejection to EM disturbances. The influence of the high voltage field has been checked by comparing the readings of sample weights with the electric field off and on; in the latter case, the effect of the ionic wind and the relevant thrust generation are suppressed by an insulating plate located below the collectors (flow stopper). The difference between these readings are lower than the final uncertainty of $\pm 5 \text{ mN}$ presented in Appendix C. The conditioner converts the mV-range signals of the cells to output signals in the 0–10V range. The outputs are connected through shielded

single-ended cables to the oscilloscope mentioned in §2, also used for the acquisition of the other signals in this experiment.

Appendix B. Measurements of the velocity field

With reference to Fig. 6, measurements of the velocity $u(y, z_c)$ along the normal direction y were initially acquired at mid-span, i.e. at the central point z_c of the z domain, in steps ranging from $\Delta y = 0.5$ mm in regions of strong velocity gradients to $\Delta y = 2$ mm where velocity shows weak changes. Then, along the spanwise direction z the velocity $u(y_i, z)$ was acquired at several different positions y_i , depending on the case at hand but always including in each cell the central point y_c equidistant from the trailing edges of two adjacent collectors. Here the step was equal to $\Delta z = 5$ mm, since no strong velocity gradients were observed along this direction. Using the velocity profiles acquired in this manner it is possible to reconstruct the output velocity field $u(y, z)$ normal to a rear cross-section of the system, i.e. to map the velocity component responsible for thrust (the moderate directional sensitivity of the pitot probe is discussed in §3.4). The ionic wind velocity u is obtained from the difference between the total pressure at the probe tip p_{tot} and the static pressure p_s , equal to the ambient pressure p_a on the measurement plane, exploiting Bernoulli theorem:

$$p_{tot} = p_s + \frac{1}{2}\rho u^2 . \quad (\text{B.1})$$

The non-ideal effects acting on the probe due to the low value of its Reynolds number and to the non-negligible air viscosity are accounted for by applying the same corrections made in [15]. The air density value ρ is obtained from ambient temperature \mathcal{T}_a and pressure p_a using the ideal gas law $p_a = \rho R_{air} \mathcal{T}_a$, where $R_{air} = 287$. J Kg⁻¹K⁻¹ is the dry air specific constant. Variations in air density due to humidity have not been taken into account because their effect was negligible.

Average values and standard deviations of the pressure time series are then used to calculate velocity from Eq. (B.1). The error propagation through Bernoulli's theorem with non-ideal corrections, calculated by RSS (Root-Square-Sum) method starting from the instruments accuracy, gives an uncertainty in the order of ± 0.015 m/s. However, the standard deviation of the velocity signal turns out to be higher because of the inherent velocity fluctuations of the flow field. In fact, the Reynolds number of the output flow may reach values in the order of $2 \cdot 10^4$ corresponding to partially developed turbulence, that affects the pitot-line-transducer system even if its frequency response is limited to few Hz. In the results of §4, the error bars include all these effects, thus are larger in presence of turbulent effects giving a simple representation of the phenomenon. Further studies with different diagnostics will be devoted to the characterization of the fluctuating part in the field of motion.

Appendix C. Measurements of thrust

The measurement principle expressed as $T = F_{off} - F_{on}$ in Eq. (1) (difference between loads with thruster off and on) can be affected by mechanical disturbances, due to the connection between the support structure and the power wiring and to vibrations from the environment, owing to the sensitivity of the system (as for EM disturbances, see Appendix A). In order to monitor the unwanted loads and validate the results, multiple acquisitions were performed for each test, tracing the load trend over time and checking the zero values before and after each acquisition set. The system of 3 cells behaves differently from a single cell because of the mechanical coupling and its overall accuracy, determined by repeated calibrations with reference weights on the unpowered system, is ± 3 mN. In turn, the statistic on repeated on-off measures as required by Eq. (1) leads then to slightly larger intervals, ranging from ± 3 to ± 5 mN, which are reported as error bars in §4. The final thrust values are reported with resolution of 0.5 mN.

Appendix D. Simplified model for determining thrust from momentum balance

In a previous work [15], the thrust per unit span T/b on a cell was estimated starting from the momentum conservation on a simplified geometry:

$$\frac{T}{b} = \int_{\mathcal{L}_{out}} \rho u^2 d\mathcal{L} - \int_{\mathcal{L}_{in}} \rho u^2 d\mathcal{L} + (p_a - p_{in})|\mathcal{L}_{out}|, \quad (\text{D.1})$$

where b is the collector or airfoil span, ρ the air density, u the velocity, p_a and p_{in} the atmospheric and inlet pressure respectively and \mathcal{L} the border of the domain, assumed 2D for simplicity. Eq. (D.1) was then applied to the domain shown in Fig. D.17, treated as a cell of an infinite array in the y direction.

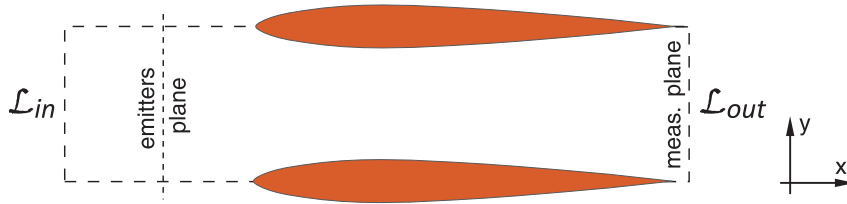


Figure D.17: Control volume used for the cell contribution in 2D thrust calculation.

The 2D approach followed in the model above implicitly introduced the hypothesis of uniform velocity distribution in spanwise direction: this hypothesis is questioned in this work, since in a strict analysis it would require collectors very wide with respect to their chord. As a consequence, a new 3D model is introduced here to account for the actual flow field, on a finite number of collectors and with a finite span.

References

- [1] J. Wilson, H. D. Perkins, W. K. Thompson, An investigation of ionic wind propulsion NASA/TM-2009-215822.
- [2] E. Moreau, N. Benard, J.-D. Lan-Sun-Luk, J.-P. Chabriot, Electrohydrodynamic force produced by a wire-to-cylinder dc corona discharge in air at atmospheric pressure, *J. Phys. D: Appl. Phys.* 46 (2013) 475204.
- [3] N. Monrolin, F. Plouraboué, O. Praud, Electrohydrodynamic thrust for in-atmosphere propulsion, *AIAA Journal* 55 (12) (2017) 4296–4305.
- [4] A. Ieta, M. Chirita, Electrohydrodynamic propeller for in-atmosphere propulsion; rotational device first flight, *J. Electrostat.* 100 (2019) 103352.
- [5] V. Khomich, V. Malanichev, I. Rebrov, Electrohydrodynamic thruster for near-space applications, *Acta Astronautica* 180 (2021) 141–148.
- [6] N. Gomez-Vega, H. Xu, J. Abel, S. Barrett, Performance of decoupled electroaerodynamic thruster, *Appl. Phys. Lett.* 118 (7) (2021) 074101.
- [7] M. Chirita, A. Ieta, First rotary ionic engine with contra-rotating propellers, *J. Propuls. Power - Article in Advance* (2022) 1–8.
- [8] G. Matsoukas, N. Ahmed, Experimental investigation of employing asymmetrical electrodes in propulsion of vehicles, in: *Evolving Energy - IEF International Energy Congress (IEF-IEC2012)*, Vol. 49 of *Procedia Eng.*, 2012, pp. 247–253.
- [9] K. Kioussis, A. Moronis, W. Fruh, Electro-hydrodynamic (ehd) thrust analysis in wire-cylinder electrode arrangement., *Plasma Sci. Technol.* 16(4) (2014) 363–369.
- [10] K. Masuyama, S. R. H. Barrett, On the performance of electrohydrodynamic propulsion, *Proc. R. Soc. A* 469 (2013) 20120623.
- [11] C. K. Gilmore, S. R. H. Barrett, Electrohydrodynamic thrust density using positive corona-induced ionic winds for in-atmosphere propulsion, *Proc. R. Soc. A* 471 (2015) 20140912.
- [12] N. Monrolin, O. Praud, F. Plouraboué, Electrohydrodynamic ionic wind, force field, and ionic mobility in a positive dc wire-to-cylinders corona discharge in air, *Phys. Rev. Fluids* 3 (6) (2018) 063701.
- [13] H. Xu, Y. He, K. L. Strobel, C. K. Gilmore, S. P. Kelley, C. C. Hennick, T. Sebastian, M. R. Woolston, D. J. Perreault, S. R. H. Barrett, Flight of an aeroplane with solid-state propulsion, *Nature* 563 (2018) 532–535.
- [14] V. Y. Khomich, I. E. Rebrov, In-atmosphere electrohydrodynamic propulsion aircraft with wireless supply onboard, *J. Electrostat.* 95 (2018) 1–12.

- [15] M. Belan, L. Arosti, R. Polatti, F. Maggi, S. Fiorini, F. Sottovia, A parametric study of electrodes geometries for atmospheric electrohydrodynamic propulsion, *J. Electrostat.* 113 (2021) 103616.
- [16] A. Ieta, R. Ellis, D. Citro, M. Chirita, J. D’Antonio, Characterization of corona wind in a modular electrode configuration, in: *Proc. ESA Annual Meeting on Electrostatics*, 2013, pp. 1–7.
- [17] E. Moreau, N. Benard, F. Alicalapa, A. Douyere, Electrohydrodynamic force produced by a corona discharge between a wire active electrode and several cylinder electrodes - application to electric propulsion, *J. Electrostat.* 76 (2015) 194–200.
- [18] M. Belan, E. Tescaroli, Discharge stability enhancement in surface corona actuators, *IEEE Trans. Plasma Sci.* 50 (2022) 69–78.
- [19] R. S. Vaddi, Y. Guan, A. Mamishev, I. Novosselov, Analytical model for electrohydrodynamic thrust, *Proc. R. Soc. A* 476 (2020) 0220.
- [20] H. Xu, N. Gomez-Vega, D. R. Agrawal, S. R. H. Barrett, Higher thrust-to-power with large electrode gap spacing electroaerodynamic devices for aircraft propulsion, *J. Phys. D: Appl. Phys.* 53 (2020) 025202.
- [21] J. Lemetayer, C. Marion, D. Fabre, F. Plouraboué, Multi-inception patterns of emitter array/collector systems in dc corona discharge, *J. Physics D: Appl. Physics* 55 (18) (2022) 185203.